Early photon tomography allows fluorescence detection of lung carcinomas and disease progression in mice in vivo

Mark J. Niedre[a,b], Ruben H. de Kleine[a], Elena Aikawa[a], David G. Kirsch[a,c], Ralph Weissleder[a], and Vasilis Ntziachristos[a,d,1]

[a]Center for Molecular Imaging Research, Massachusetts General Hospital, Harvard Medical School, Charlestown, MA 02129; [b]Department of Electrical and Computer Engineering, Northeastern University, Boston, MA 02115; [c]Department of Radiation Oncology, Duke University, Durham, NC 27710; and [d]Institute for Biological and Medical Imaging, Technical University of Munich and Helmholtz Center Munich, Ismaningerstrasse 21, D-85764 Munich, Germany

Edited by Britton Chance, University of Pennsylvania School of Medicine, Philadelphia, PA, and approved October 7, 2008 (received for review May 16, 2008)

Imaging of targeted fluorescent probes offers significant advantages for investigating disease and tissue function in animal models in vivo. Conversely, macroscopic tomographic imaging is challenging because of the high scatter of light in biological tissue and the ill-posed nature of the reconstruction mathematics. In this work, we use the earliest-transmitted photons through Lewis Lung Carcinoma bearing mice, thereby dramatically reducing the effect of tissue scattering. By using a fluorescent probe sensitive to cysteine proteases, the method yielded outstanding imaging performance compared with conventional approaches. Accurate visualization of biochemical abnormalities was achieved, not only in the primary tumor, but also in the surrounding tissue related to cancer progression and inflammatory response at the organ level. These findings were confirmed histologically and with ex vivo fluorescence microscopy. The imaging fidelity demonstrated underscores a method that can use a wide range of fluorescent probes to accurately visualize cellular- and molecular-level events in whole animals in vivo.

cancer | optical | diffuse | molecular | imaging

Pioneering developments in the engineering of fluorescent proteins, probes, and the chemistry of nanomaterials and fluorochromes have enabled in vivo imaging of cells and their constituents in unperturbed environments in recent years (1, 2). Fluorescent proteins have become essential reporter molecules of gene expression and regulation, protein function, and cell motility in living organisms (3–5). Likewise, extrinsically administered fluorescent probes have demonstrated high sensitivity in targeting specific cells [for example, cancer cells (5)] or identifying proteins and molecular pathways of development, function, and disease in vivo. Further enhanced by sensing of spectrally separated fluorescent molecules, fluorescence microscopy currently offers unparalleled insights in the study of cellular and protein interactions. In principle, fluorescence technology could be similarly used to study normal and diseased tissues at the whole-organ and live-animal level. However, there remain significant challenges in imaging beyond a few hundred micrometers in depth because of the high degree of light scatter in tissues, which arises from photon interactions with cellular membranes and organelles. Currently, fluorescence macroscopic imaging is largely performed by illuminating tissue at the fluorochrome's excitation wavelength and detecting the emission from within the animal's body by using appropriate spectral filters. Photographic and planar-fluorescence-imaging implementations of this approach offer only 2-dimensional views and largely qualitative data, because they do not consider the nonlinear relation of photon strength to lesion depth and tissue optical properties. In response, tomographic approaches have been developed to overcome the limitations of these methods (6–8). Optical tomography utilizes multiprojection measurements and physical models of photon propagation to quantitatively retrieve fluorochrome biodistribution in tissues. However, the physical limits of imaging performance of current tomographic implementations ultimately depend on the tissue optical properties—primarily scattering—which leads to a highly ill-posed (i.e., inaccurate) inverse problem that reduces the spatial resolution and yields images that are highly dependent on the particulars of the reconstruction algorithm used.

To develop a next-generation optical tomographic method that can selectively reduce the effects of tissue scattering to improve imaging accuracy, we developed a system to use early arriving photons, that is, photons emitted from an ultrafast laser source (i.e., pulse width <1 ps) that propagate through tissue and are the first to arrive at a time-gated detector a distance away from the source (9–16). The scattering of these early photons is strongly biased in the forward direction and correspondingly they experience a lower number of total scattering events. As a result, they preferentially propagate along significantly less diffusive paths connecting the source and the detector versus ungated photons and can therefore be used to significantly improve imaging resolution. Early photons have been used previously in planar transillumination studies of breast tissue samples (9, 10). The use of early photons in combination with theoretical models of early-photon propagation have also been considered in the past and yielded systems with the ability to localize relatively simple objects such as 1 or 2 absorbing or fluorescent spheres embedded in a homogenous scattering fluid (13, 14) or, as in our previous work, complex shaped absorbing optical phantoms (15, 16). These methods, however, were never extended to in vivo imaging and consequently they have not been shown to be biologically useful.

Here, we use early-photon technology for performing high-fidelity fluorescence tomography in living tissues. The imaging approach differed from previous work in that it used (*i*) high-spatial sampling of photon fields and projections over 360° view angles, similar in implementation to X-ray CT, but using near-infrared photons; (*ii*) a dual-wavelength data-normalization scheme that proved necessary for imaging in tissue-related optical heterogeneity; and (*iii*) a corresponding theoretical model that allowed accurate modeling of light propagation in tissue at early times. It was further found that despite the significant photon rejection associated with the utilization of early photons, this implementation can operate at signal-to-noise ratio (SNR) statistics virtually identical to methods using all available photons (e.g., versus continuous-wave techniques) but at a significantly higher imaging fidelity. Applied in vivo to imaging tumoral proteases, early-photon tomography (EPT) was further shown to be capable not only of reproducibly reconstructing protease activity in primary tumors, but also of detecting

Author contributions: M.J.N., R.H.d.K., and V.N. designed research; M.J.N., R.H.d.K., and E.A. performed research; M.J.N., D.G.K., R.W., and V.N. contributed new reagents/analytic tools; M.J.N., E.A., and V.N. analyzed data; and M.J.N. and V.N. wrote the paper.

The authors declare no conflict of interest.

This article is a PNAS Direct Submission.

[1]To whom correspondence should be addressed. E-mail: v.ntziachristos@tum.de.

This article contains supporting information online at www.pnas.org/cgi/content/full/0804798105/DCSupplemental.

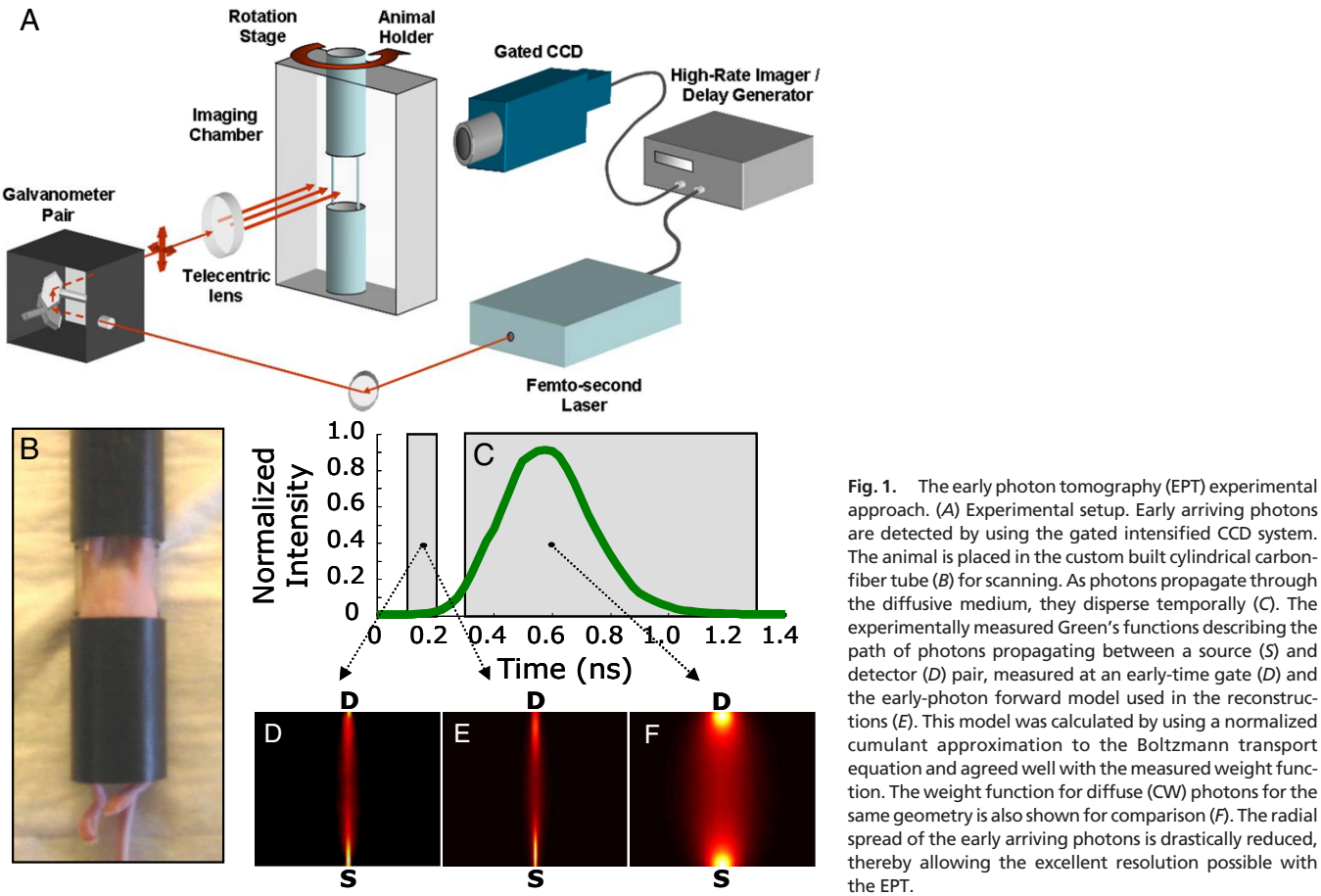

Fig. 1. The early photon tomography (EPT) experimental approach. (*A*) Experimental setup. Early arriving photons are detected by using the gated intensified CCD system. The animal is placed in the custom built cylindrical carbon-fiber tube (*B*) for scanning. As photons propagate through the diffusive medium, they disperse temporally (*C*). The experimentally measured Green's functions describing the path of photons propagating between a source (*S*) and detector (*D*) pair, measured at an early-time gate (*D*) and the early-photon forward model used in the reconstructions (*E*). This model was calculated by using a normalized cumulant approximation to the Boltzmann transport equation and agreed well with the measured weight function. The weight function for diffuse (CW) photons for the same geometry is also shown for comparison (*F*). The radial spread of the early arriving photons is drastically reduced, thereby allowing the excellent resolution possible with the EPT.

tissue biochemical changes in adjacent lung tissue. These appeared to be indicative of disease progression in the adjacent tissue and the associated inflammatory response. The biochemical information yielded by EPT was therefore highly complementary to the high-resolution structural information obtained by using correlative X-ray CT.

Results and Discussion

The EPT system is shown in Fig. 1 and is capable of collecting photon fields propagating through tissue over 360° projections in a time-gated mode. The resolution improvement of this implementation over approaches using light of constant intensity has been studied with absorbing phantoms embedded in diffusive media by using an earlier system prototype (15, 16) operating in attenuation mode. Mice were placed into the imaging chamber inside a custom-made cylindrical holder consisting of 2 carbon-fiber tubes that supported the upper and lower body, connected to each other with 2 carbon fiber rods to allow clear viewing of the animal's torso (Fig. 1*B*). The tube was immersed into a 2.2-cm-wide imaging chamber and surrounded by an optical matching fluid; the mouse head was above fluid level. The use of a matching fluid was not obligatory as in ultrasonic imaging, but allowed relaxation of experimental requirements for this work. The sample was then rotated over 360° in 5° increments, so that single axial slices of the animal were scanned at a time by using a row of 27 beam positions separated by 0.8 mm for each slice acquired. For each animal, multiple axial slices were scanned at different locations along the animal's torso. The early-photon intensities transmitted through the animal were captured by using a high-speed gated image intensified CCD (see *Materials and Methods*). The imager was synchronized to the femtosecond laser with the 80 MHz output trigger of the source, and each image was taken during a temporal gate after a fixed delay following the laser pulse. This gate was set to 100 ps after the time representing the arrival of a laser pulse onto the front glass window of the chamber, assuming free-space propagation through the imaging chamber. This particular time gate was selected for this model because it was the earliest temporal window to yield measurements with ≈23 dB SNR, which was found experimentally to be the minimum SNR requirement for high-fidelity image reconstruction. This SNR level was determined by using the standard definition $\mathrm{SNR}_I = 20{\cdot}\log_{10}(\mu_I/\sigma_I)$, where μ_I and σ_I are the mean and standard deviation of 100 early-photon measurements collected for the 100-ps gate through a diffusive fluid with a 200-ms CCD camera exposure time (corresponding to 1.6×10^7 laser pulses) using a single on-axis source-detector pair.

Transmitted early-photon measurements were made both at the excitation wavelength of the laser and at the fluorescence emission wavelength of the protease-imaging probe (Prosense-750; see *Materials and Methods*). It should be noted that, somewhat counterintuitively, the temporal kinetics of the early portion of the fluorescence emission curve are dominated by the photon propagation through the media as opposed to the fluorescence decay lifetime of the fluorochrome (13). Therefore, the early arriving excitation and emission photons arrive at the detector at approximately the same time gate. Images from the gated-CCD camera were segmented into an array of virtual detectors in postprocessing. The intensities of the virtual detector directly opposite from the source positions were used for each projection. The fluorescence data were normalized to the intrinsic data according to the normalized Born ratio (17), an operation that virtually cancels the effects of the variation

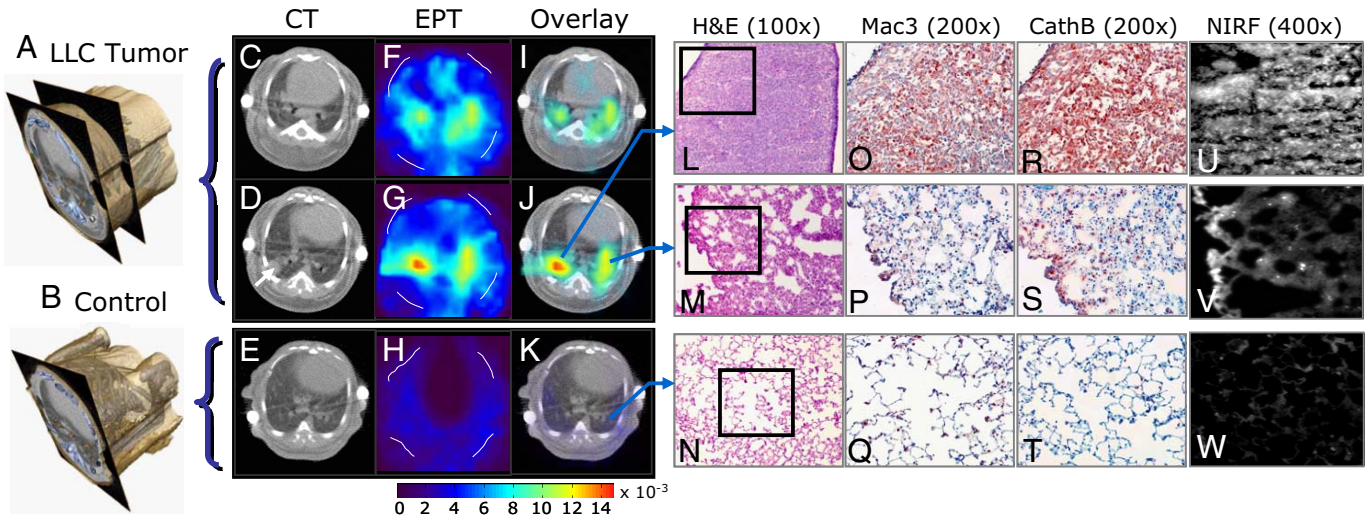

Fig. 2. EPT imaging of a Lewis Lung Carcinoma tumor model in mice. (*A* and *B*) Three-dimensional rendering of a mouse with an LLC tumor 8 days after inoculation and a wild-type control. Mice were injected with a cathepsin-activatable probe (Prosense-750) 24 h before scanning with the EPT system. (*C–E*) Selected axial CT slices from the 2 mice. The 2 white circles on either side of the mouse are from the carbon-fiber holder. (*F–H*) Axial EPT reconstructions corresponding to the CT slices (arbitrary units). (*I–K*) Overlay of the EPT reconstruction on the CT slice. Histology was performed on excised lung samples. (*L–N*) H&E stain of tumor, lung tissue that was contralateral to the tumor tissue, and normal lung tissue, respectively. (*O–Q*) Macrophage-3 stain and (*R–T*) cathepsin B stain of the same tissue. Near-infrared fluorescence (NIRF) microscopy was also performed on adjacent tissue sections (*U–W*). The increased macrophage, cathepsin B, and NIRF levels in the primary tumor and the contralateral side corroborates the increased fluorescence signal from the protease-activatable probe measured with the EPT system. As discussed in the text, the increased fluorescence in the contralateral side was primarily due to the host inflammatory response of the lung in response to tumoral challenge as well as microscopic growth of LLC cancer cells into normal tissue. The fluorescent streaks emanating from the side of the animal are reconstruction artifacts.

of optical properties and index of refraction along the path of photon propagation on the fluorescence signal collected. This data-processing step is critical because it compensates for the large optical heterogeneity in the torso of the animal.

As the 100-fs laser pulse propagates through the 2.2-cm imaging chamber, the pulse broadens drastically to ≈1.5 ns (Fig. 1*C*). To describe the propagation of the early arriving photons, a cumulant approximation to the Boltzmann transport equation was used (18, 19) and by using normalization of the photon density to the intrinsic photon propagation between the source–detector pair. This approximation is more accurate than time-resolved diffusion theory at early times (13, 14), because it correctly models the propagation of ballistic photons and early-diffuse photons at early-time gates. We have experimentally validated this early-photon propagation model by using experimental measurements of the 3-point Green's function through the medium. The Green's function for a source–detector pair was derived by stepwise translation of an absorber through an intralipid-filled imaging chamber and measurement of the effect of the absorber placed on different locations in the medium on the measured signal intensity. The experimentally measured weight function for early photons, the early-photon theoretical forward model, and the corresponding forward model for a continuous wave (CW) photon source are shown in Fig. 1 *D–F* for comparison. The strongly reduced width of the Green's function by using early photons versus CW photons is the key aspect, not only to improved resolution of the EPT system, but also to the overall betterment in imaging fidelity, because the inverse problem becomes significantly less ill-posed compared with CW implementations. The distribution of the activated fluorescent probe was calculated by solving the resulting inverse problem by using custom-written software (see *Materials and Methods*).

To test the performance of EPT technology *in vivo*, the right inferior lobes of the lungs of female nude mice were inoculated with LLC tumors, a rapidly infiltrating carcinoma that originated from a spontaneous carcinoma in a C57BL mouse. It has been shown previously that this model (20) as well as other lung tumor models (21) have markedly up-regulated levels of cysteine proteases during tumor growth. Therefore, in this study we used an activatable probe (Prosense-750; Visen Medical), which is nonfluorescent at base state but becomes fluorescent on interaction with cysteine proteases—primarily cathepsin B and to a lesser degree cathepsins S, L, and K (22). The lung was selected for imaging because it is a particularly challenging organ to image by using optical techniques because of the high optical scatter of the organ, as well as the high absorption of the adjacent blood-rich heart region and the enclosure in the rib cage that overlay the lungs in all optical projections through the mouse torso (23). In general, although EPT images accurately resolved increased protease activity in the primary tumors, they also yielded additional areas of high fluorescence activity that did not have corresponding masses visible on the CT images. An example is shown in Fig. 2, wherein sample reconstructed slices from a mouse imaged 8 days after inoculation with an LLC tumor and from a control animal are shown. X-ray CT reconstructions and axial images obtained from the mice are shown (Fig. 2 *A–E*), as well as the corresponding EPT fluorescence reconstructions from the same slices (Fig. 2 *F–H*). Areas of the highest fluorescence intensity shown on the reconstructed images were congruent with the tumor appearance on X-ray CT images. In addition, tissue adjacent to the tumor region and on the contralateral (left) lobe of the lung that appeared nominally tumor-negative on the X-ray CT scans also showed elevated fluorescence compared with the activity reconstructed in control animals.

To investigate the source of fluorescence, histopathological and immunohistochemical examination of the tissue was performed (Fig. 2 *L–T*). Immunohistochemical stains with cathepsin B and macrophage (Mac-3) antibodies were performed along with standard H&E staining. As anticipated, the tumor tissue showed dense packing of cells with high expression of cathepsin B and highly elevated Mac-3 levels (22, 24). Cathepsin-B-expressing macrophages have previously been shown to activate Prosense (25). The tissue from the lobe contralateral to the tumor tissue also showed up-regulated levels of cathepsin B but comparable levels of Mac-3 staining relative to the normal control tissue, suggesting an inflammatory host response of the normal lung tissue (26). Tissues adjacent to tumors were further found morphologically abnormal, showing thick walls of the alveoli and denser packing of cells. The

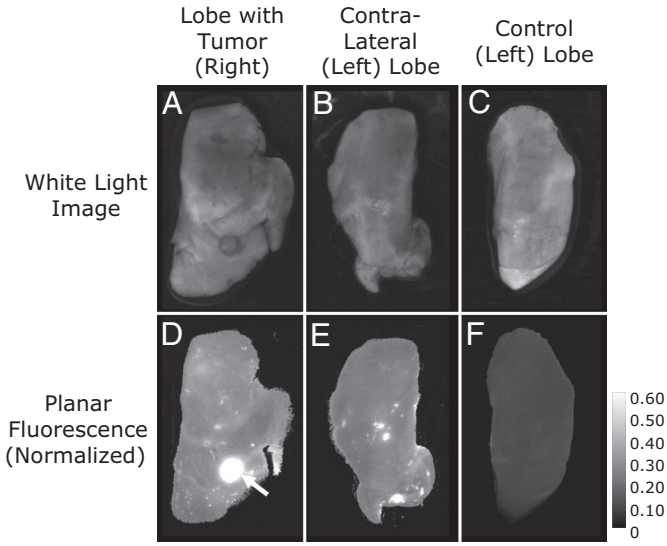

Fig. 3. Tumor-bearing (LLC tumor, 8 days after inoculation) and control mice were injected with the cathepsin-activatable probe Prosense-750 24 h before EPT imaging. After tomographic imaging they were immediately killed and dissected for surface-reflectance imaging. White light reflectance images of excised right (*A*) and left (*B*) lobes of the lung of a mouse with an LLC tumor and from a control mouse (*C*) are shown, as well as normalized planar-fluorescence images of the same lung tissue (*D–F*). The fluorescence was most intense in the tumor, and other microfoci, but was globally present at elevated levels throughout the entire organ versus controls. The time required for epiluminescence imaging herein resulted in significant microscopic degradation of the lung tissue so that subsequent immunohistochemical analysis of the tissue was impossible.

increased fluorescence was not due to an inflammatory response resulting from the mechanical injury of the LLC tumor inoculation, because EPT and planar fluorescence imaging of animals injected with media only showed no increased fluorescence versus uninjected controls (data not shown). Further immunohistochemical analysis with tumor-associated antibodies—specifically, E-cadherin and N-cadherin (27)—indicated that the adjacent tissue most likely contained infiltrating LLC cancer cells that had not yet developed into full tumors, consistent with the aggressive nature of the tumor growth. A neutrophil stain further showed that host inflammatory response was present in response to the cancer cells (supporting information (SI) Fig. S1). Higher-magnification images of the tumor tissue are shown in Fig. S2.

Planar-reflectance fluorescence imaging of surgically excised lung tissue postmortem confirmed that the fluorescence signal was not confined to the tumor, but was also present in the adjacent tissue and contralateral lobe of the lung. Compared with ex vivo measurements from control lungs, the fluorescence signal was found to extend throughout the lung of challenged mice, not only in isolated microfoci (Fig. 3 *A–F*). Near-infrared fluorescence microscopy of the excised tissue also demonstrated increased fluorescence (and protease activity) in the contralateral lobe of the lung versus normal lung (Fig. 3 *G–I*). In summary, fluorescence EPT reconstructions sensitively detected not only elevated activated protease expression in the tumor but in the entire lung, most likely indicative of a systemic response of lung tissue to the local tumoral challenge and to microscopic cancer growth. This experiment demonstrates the ability of EPT to yield synergistic biochemical information to that obtained with high-resolution X-ray CT.

We have further observed a similar effect in a second lung tumor model, specifically in transgenic LSL-KrasG12D mice that express oncogenic K-ras after infection with an adenovirus containing Cre-recombinase (21) (see Fig. S3). With this model, multiple, significantly smaller (≈0.5–2.0 mm diameter) primary tumors developed over a period of months after adenoviral infection. Similar to the LLC model, EPT imaging with Prosense-750 revealed fluorescence activity throughout the entire challenged lung that was verified through planar fluorescence imaging. Immunohistochemical analysis of the excised tissue revealed abnormal morphology, up-regulated levels of cathepsin B and increased macrophage content, both in primary tumors and in adjacent tissue, in this case suggesting neoplastic progression in the adjacent tissue (26). In summary, imaging in both lung tumor models demonstrated the ability of EPT to yield biochemical information indicative of disease progression that was complementary to that obtained with high-resolution X-ray CT.

To investigate the ability of the EPT system to follow tumor growth in vivo, we performed a series of longitudinal studies on an additional 6 animals with implanted LLC tumors. Before these experiments, we verified that Prosense-750 was completely cleared from lung tissue 4 days after initial injection of the probe. Hence, mice were imaged at 4-day intervals after tumor inoculation. Fig. 4 *A–F* shows example CT and EPT images of tumor progression at 4-day intervals from the same mouse. This was repeated for all 6 animals, and the reconstructed tumor volumes determined with EPT fluorescence imaging (defined as the extent of the FWHM signal interpolated between each slice) were compared with those from CT imaging (Fig. 4*G*) where tumors were visible, showing good correlation between the 2 modalities; the slope of Fig. 4*G* indicates that the EPT volume was larger by a factor of ≈2 compared with the X-ray CT images, consistent with our observation that the fluorescence signal extends beyond the margin of the bulk tumor. From these experiments, it was further determined that the tumors were visible with the EPT system ≈4 days after tumor inoculation, which was equivalent to a minimum size of ≈0.02 cm (3).

In this work, we have performed a demonstration of the early-photon tomography (EPT) concept in murine lung tumor models in vivo. In the current implementation, the photons collected arrive within the first 100 ps from the assumed arrival time of nonscattered photons, that is, photons propagating in water. The utilization of this time gate rejects ≈99% of the total photons available, which at

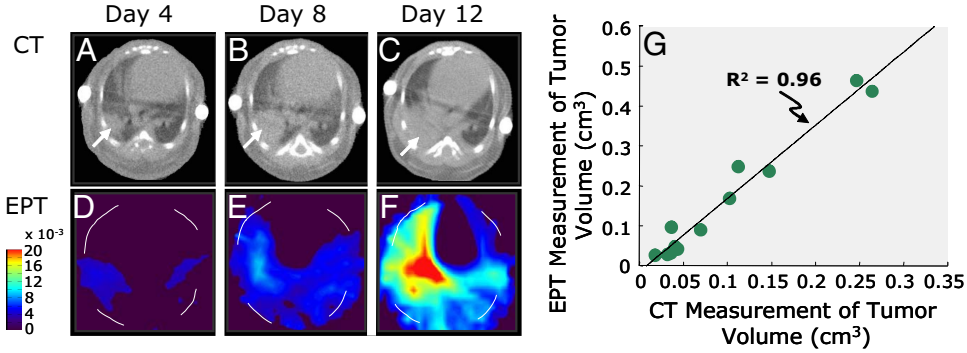

Fig. 4. Longitudinal EPT imaging study measuring growth of LLC tumors in individual animals at 4-day intervals ($n = 6$). (*A–C*) Example X-ray CT axial slices at days 4, 8, and 12, from a single animal; (*D–F*) EPT reconstructions corresponding the CT axial slices in the same animal. (*G*) An excellent correlation was observed between the tumor volume calculated with the EPT system versus CT imaging. Tumors could be resolved with EPT after 4 days, corresponding to a minimum detectable tumor size of ≈0.02 cm (3).

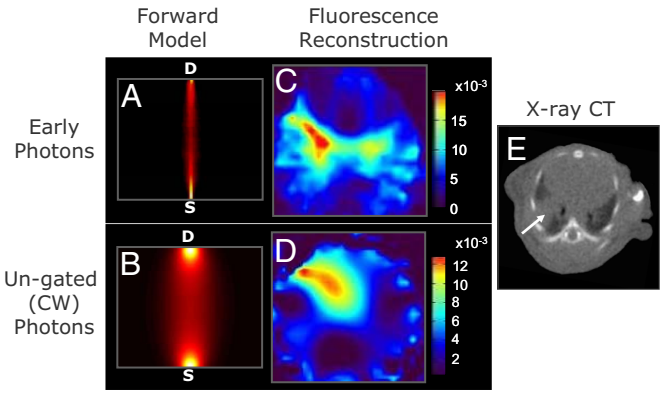

Fig. 5. Fluorescence reconstructions obtained by using early arriving photons compared with ungated (continuous-wave) photons in a mouse with an LLC tumor, 10 days after injection. The forward model for early arriving photons and ungated photons are shown (*A* and *B*) as well as the fluorescence reconstructions for the axial slice (*C* and *D*), and the corresponding X-ray CT axial slice (*E*). The use of early photons enables fluorescence reconstructions with superior resolution and localization of the activated fluorophore in the right lobe of the lung, as well as on the contralateral side compared with the ungated reconstruction.

first implies that the benefits of improved imaging resolution come at the expense of detection sensitivity. However, a constant-intensity tomography method requires the use of off-axis projections for stabilizing the inversion problem (28). In this case, an appropriate experimental comparison that incorporates all data collected in CW mode within a radius around the on-axis detector (typically 1 cm), calculated the equivalent average SNR in CW mode, assuming the same incident power as in EPT and found it to be 25dB, vs. 23dB used herein. Therefore, the EPT tomographic problem operates with only slightly reduced photon statistics compared with a CW problem, despite the high rejection of photons, because of the inversion specifics of the 2 tomographic cases. This finding further explains the high detection sensitivity observed in the in vivo measurements. Correspondingly, inversions performed by using the same animal model but without operating the intensified CCD in time-gated mode (i.e., the equivalent to using sources of constant intensity) resulted in significantly poorer localization accuracy and image resolution (Fig. 5) and lack of detection sensitivity of biochemical changes, especially in the contralateral lung. It should be noted that this is not a direct comparison of EPT and fluorescence molecular tomography (FMT), because the latter generally utilizes much larger datasets (in particular, from photons detected off-axis from the source) in image reconstruction. Rather, this experiment demonstrates the value of time-gating in effectively reducing the scatter of the detected photons. Although the CW method has been previously shown to localize point-like fluorescent contrast, the EPT method developed herein goes beyond localization and offers an accomplished imaging modality that can accurately reconstruct distributed activity as well.

Conclusion

In summary, we have combined detection of early photons in high spatial sampling 360° geometries with data normalization and inversion methods and demonstrated that the resulting tomographic modality can be used to 3-dimensionally image fluorescence-based molecular signatures in murine lungs with superior fluorescence tomographic imaging performance, yielding high fidelity and sensitivity. EPT is therefore expected to advance the application performance of whole-body optical tomography of small animals. The improved imaging merits of the technology resulted in the detection of primary tumors, but also systemic biochemical changes in the entire challenged lung, in this case yielding complementary information to that obtained with standard X-ray CT. We have demonstrated that fluorescence-based tomographic detection can be used to study solid tumors and early pathological responses in adjacent tissue in vivo through intact animals by using early arriving photons, with superior imaging performance over the current state of the art. Because the thoracic cavity is among the most highly optically scattering regions of the mouse anatomy, we anticipate that EPT will potentially perform even better in organs that exhibit less scatter, such as the liver or brain. Detection of time-resolved photon profiles has been shown feasible in the past through larger tissues and organs such as the human breast (29); hence, use of an early-photon detection scheme conceptually similar to the one shown herein may further prove to be a useful approach to improving the image quality achievable in larger animals or in humans, although this would require optimization of the instrumentation, detection gates, and inversion algorithms for larger volumes.

Materials and Methods

Forward Models. The computed forward model for photon propagation between a source–detector pair at early time gates required an accurate description of the early arriving photons consisting of ballistic and mildly diffusive components. The normalized early-photon field at a measurement time t after the laser pulse was calculated as follows (11):

$$U^n(r_s, r_d, t) = Q \cdot \frac{1}{G(r_s, r_d, t)} \int_0^t \int G(r, r_d, t-\tau) \cdot \frac{n(r)\cdot\nu}{D} \cdot G(r_s, r, \tau) \cdot d\tau \cdot d^3r \qquad [1]$$

where Q is a gain factor associated with the different gains of the system in the emission and excitation wavelengths, r is the position inside the diffuse media, r_s and r_d are the source and detector positions of each source–detector pair, respectively, $n(r)$ is the concentration of the fluorophore in the tissue volume, ν is the speed of light in the medium, and D is the diffusion coefficient. For our application, the ballistic (unscattered) contribution is essentially zero because of the relatively thick tissue volume used so that it is strongly dominated by the ''early-diffuse'' component. Normalization of the forward model with the calculated transmitted intensity between the source–detector pair [i.e., $G(r_s, r_d, t)$], follows after the corresponding normalization of the fluorescence measurement with a measurement representative of photon propagation in the medium and is necessary for accurate reconstruction in optically heterogeneous media in analogy to improvements seen in constant wave fluorescence tomography (17).

The Green's function G was given by the photon density calculated by using the cumulant solution to the Boltzmann transport equation (18, 19):

$$N(r, t) = \frac{1}{(4\pi D_{zz} c t)^{1/2}} \frac{1}{4\pi D_{xx} c t} \exp\left[-\frac{(z - R_z(t))^2}{4 D_{zz} c t}\right] \times \exp\left[-\frac{(x^2 + y^2)}{4 D_{xx} c t}\right] \exp(-\mu_a t) \qquad [2]$$

where $R_z(t)$ is the moving center of the photon source, D_{xx} and D_{zz} are the directional diffusion coefficients defined in detail elsewhere (18, 19). This equation accurately describes the propagation of photons at early-time gates by allowing modeling of the forward-biased scattered of the light, as opposed to isotropic scattering as in the continuous wave case. The optical properties of the media (i.e., μ_s' and μ_a) were predetermined by using fitting of the time- and spatially resolved photon profiles as described in ref. 23 and were assumed to be equal for both the excitation and emission photons.

The calculated weight function was corrected for the finite (1 mm) virtual detector size arising from segmenting of the CCD image and the result was further convolved with the temporal impulse–response function of our imaging system, so that the appropriate forward model for a given time gate could be calculated. For this work, the time gate used was 100 ps after the free-space propagation time of the laser pulse through the imaging chamber.

System Description. A pulsed, femtosecond laser (MaiTai, Spectra-Physics) operating at 732 nm with an 80 MHz repetition rate and a 100-fs pulsewidth was free-beam coupled into a scanning galvanometer mirror pair, so that the power at the surface of mouse was ≈70 mW. By using this arrangement, the laser beam could be translated across the imaging chamber with a better than 30-μm positional accuracy without significant pulse broadening (<100 fs). Mice were placed in a custom-built carbon-fiber tube that was mounted in a rotation stage (Newport PR50 Series with ESP300 Motion Controller; Newport). Transmitted light was detected with a 12-bit gated-image intensifier (LaVision Picostar, Lavision) with a 200-ps imaging gate width and 25-ps time step. Spectral selection of the intrinsic (excitation) and fluorescent light was achieved by using a 10-nm bandpass interference filter centered at 740 nm (Andover) and a long-pass filter with a cut-on wavelength of 770 nm (Andover), respectively.

Data Analysis/Image Reconstruction. The image reconstruction strategy generally followed those published by our group previously (7, 8). In brief, the system geometry was discretized with a 0.5- × 0.5-mm mesh per slice. A vector $\boldsymbol{y}$ containing sets of normalized source–detector pairs was related to the unknown fluorochrome concentration in each of the mesh nodes, described by a vector $\boldsymbol{x}$, using a matrix equation $\boldsymbol{y} = \boldsymbol{W}\cdot\boldsymbol{x}$, where $\boldsymbol{W}$ is the sensitivity matrix given by the forward model described above. Inversion of the matrix equation was performed by using singular value decomposition (SVD) with Tikhonov regularization. Inversions required ≈15 s on a 2.8 MHz Pentium 4 personal computer by using the Matlab software package (Mathworks) and custom-written software.

Inoculation of Lung Tumors. All animal studies were performed according to procedures approved by the Massachusetts General Hospital Review Board. A total of 15 female nu/nu mice (COX7, Massachusetts General Hospital, Boston, MA) aged 6–10 weeks were used in the imaging studies. Lewis lung carcinoma (LLC) cells were grown at 37 °C in 5% CO_2 in Dulbecco's modified Eagle's medium with 10% heat-inactivated FBS plus 1% glutamine, penicillin, and streptomycin (20). A 10-μL aliquot of 10^6 LLC cells in suspension was injected into the right inferior lobe of the lung through a skin incision. Wound closure by using a standard suture was performed. Tumors were allowed to grow up to a maximum of 14 days before killing the animal.

Animal Handling and Image Acquisition. Twenty-four hours before EPT imaging, the animals were i.v. injected with 2 nmol of Prosense-750 (Visen Medical). Prosense-750 is a near-infrared Alexa-fluor 750-based, fluorescent-activatable probe that becomes active when cleaved by a number of cysteine proteases, in particular, cathepsin B, and to a lesser degree by cathepsins S, L, and K. Mice were anesthetized by i.p. injection of 10 mg/kg xylazine and 90 mg/kg ketamine and then were placed into the cylindrical carbon-fiber tube described in the main text so that they could be easily immobilized and rotated for EPT imaging. The liquid matching solution used comprised 1.75% intralipid (prepared from a stock solution of 10% Intralipid; Baxter Healthcare) and 87.5 ppm ink (Higgins Ink, Sanford). The matching solution was warmed and periodically exchanged to prevent hypothermia of the animal during imaging. The total imaging time with the current imaging system was ≈45 min per animal, but we anticipate that optimization of the system design in next-generation implementations will reduce the scan time significantly through the use of, for example, parallel illumination of multiple beams, or plane wave illumination.

X-Ray Computed Tomography. X-ray CT images were acquired on a combined high-resolution, single-photon emission CT (SPECT) scanner (Gamma-Medica, X-SPECT). Mice were anesthetized by i.p. injection of a xylazine/ketamine mixture before scanning and placed inside the carbon-fiber tube so that the EPT fluorescence and CT images could be overlaid. A total of 256 projections were acquired for each mouse, and reconstructions were performed with a filtered back-projection algorithm. Visualizations and 3D renderings of CT data were performed with the Amira (Mercury-TGS) and Image-J software packages.

Histological Analysis. Lungs were excised from the mice after EPT scanning and carefully reinflated by using ≈0.5 mL of OCT compound (Tissue-Tek OCT compound, Sakura Finetek). After dissection the lungs were snap-frozen in OCT compound. Tissue samples were cut into 6-μm-thick slices and stained with H&E for overall morphology. Immunohistochemistry was performed on sections by using anti-cathepsin B (Santa Cruz Biotechnology) antimacrophage (Mac3, BP Pharningen) antibodies with the avidin-biotin peroxidase method. Supplemental histological analysis was also performed by using anti-E-cadherin, anti-N-cadherin (murine reactive; Cell Signaling) and antineutrophil (murine reactive; Abcam) antibodies. The reaction was visualized with a 3-amino-9-athyl-carbazol substrate (AEC, Sigma), yielding red reaction products. Adjacent sections treated with nonimmune IgG provided controls for antibody specificity. Images were captured with a digital camera (Nikon DXM 1200-F, Nikon). Near-infrared fluorescence microscopy was performed on sections of unstained tissue by using an upright epi-fluorescence microscope (Nikon 80i equipped with Cy7/AF750 filter set; Nikon).

ACKNOWLEDGMENTS. The authors thank Gordon Turner for his contribution, Giannis Zacharakis for help in hardware development, Kelly Kristoff for assistance in cell culture, Vincent Lok for assistance in histological preparation, and Jose Figuiredo for assistance in animal surgery. This work was supported in part by National Institutes of Health Grant RO1 EB 000750 and by the National Cancer Institute of Canada through the Terry Fox Foundation (M.N.).

1. Herschman HR (2003) Molecular imaging: Looking at problems, seeing solutions. *Science* 302:605–608.
2. Massoud TF, Gambhir SS (2003) Molecular imaging in living subjects: Seeing fundamental biological processes in a new light. *Genes Dev* 7:545–580.
3. Ntziachristos V, Ripoll J, Wang LV, Weissleder R (2005) Looking and listening to light: The evolution of whole body photonic imaging. *Nat Biotechnol* 23:313–320.
4. Giepmans BN, Adams SR, Ellisman MH, Tsien RY (2006) The fluorescent toolbox for assessing protein location and function. *Science* 312:217–224.
5. Jiang T, *et al.* (2004), Tumor imaging by means of proteolytic activation of cell-penetrating peptides. *Proc Natl Acad Sci USA* 101:17867–17872.
6. Hebden JC, *et. al* (2005) Imaging changes in blood volume and oxygenation in the newborn infant brain using three-dimensional optical tomography. *Phys Med Biol* 49:1117–1130.
7. Graves EE, Ripoll J, Weissleder R, Ntziachristos V (2003) A submillimeter resolution fluorescence molecular imaging system for small animal imaging. *Med Phys* 30:901–911.
8. Ntziachristos V, Tung CH, Bremer C, Weissleder R (2002) Fluorescence molecular tomography resolves protease activity in vivo. *Nat Med* 8:757–761
9. Wang L, Ho PP, Liu C, Zhang G, Alfano RR (1991) Ballistic 2-D imaging through scattering walls using an ultrafast optical Kerr gate. *Science* 253:769–771.
10. Berg R, Jarlman J, Svanberg S (1993) Medical transillumination imaging using short-pulse diode lasers. *Appl Opt* 32:554–558.
11. Cai W, *et al.* (1996) Time-resolved optical diffusion tomographic image reconstruction in highly scattering turbid media. *Proc Natl Acad Sci USA* 93:13561–13564.
12. Ni X, Xing Q, Cai W, Alfano RR (2003) Time-resolved polarization to extract coded information from early ballistic and snake signals through turbid media. *Opt Lett* 28:343–345.
13. Wu J, Perelman L, Dasari RR, Feld MS (1997) Fluorescence tomographic imaging in turbid media using early-arriving photons and Laplace transforms. *Proc Natl Acad Sci USA* 94:8783–8788.
14. Chen K, Perelman LT, Zhang Q, Dasari RR, Feld MS (2000) Optical computed tomography in a turbid medium using early arriving photons. *J Biomed Opt* 5:144–154.
15. Turner GM, Zacharakis G, Soubret A, Ripoll J, Ntziachristos V (2005) Complete-angle projection diffuse optical tomography by use of early photons. *Opt Lett* 30:409–411.
16. Turner GM, Soubret A, Ntziachristos V (2007) Inversion with early photons. *Med Phys* 34:1405–1411.
17. Soubret A, Ripoll J, Ntziachristos V (2005) Accuracy of fluorescent tomography in the presence of heterogeneities: Study of the normalized Born ratio. *IEEE Trans Med Imaging* 24:1377–1386.
18. Cai W, Lax M, Alfano RR (2000) Cumulant solution of the elastic boltzmann transport equation in an infinite uniform medium. *Phys Rev E* 61:3871–3876.
19. Xu M, Cai W, Lax M, Alfano RR (2002) Photon migration in turbid media using a cumulant approximation to radiative transfer. *Phys Rev E* 65:066609.
20. Figueiredo JL, Alencar H, Weissleder R, Mahmood U (2006) Near infrared thoracoscopy of tumoral protease activity for improved detection of peripheral lung cancer. *Int J Cancer* 118:2672–2677.
21. Grimm J, *et al.* (2005) Use of gene expression profiling to direct in vivo molecular imaging of lung cancer. *Proc Natl Acad Sci USA* 102:14404–14409.
22. Weissleder R, Tung CH, Mahmood U, Bogdanov A (1999), In vivo imaging of tumors with protease-activated near-infrared fluorescent probes. *Nat Biotech* 17:375–378.
23. Niedre MJ, Turner GM, Ntziachristos V (2006) Time-resolved imaging of optical coefficients through murine chest cavities. *J Biomed Opt* 11:064017.
24. Bogdanov AA Jr, Lin CP, Simonova M, Matuszewski L, Weissleder R (2002), Cellular activation of the self-quenched fluorescent reporter probe in tumor microenvironment. *Neoplasia* 4:228–236.
25. Nahrendorf M, *et al.* (2007), Dual channel optical tomographic imaging of leukocyte recruitment and protease activity in the healing myocardial infarct. *Circ Res* 100:1218–1225.
26. Coussens LM, Werb Z (2002) Inflammation and cancer. *Nature* 420:860–867.
27. Abutaily AS, Addis BJ, Roche WR (2002) Immunohistochemistry in the distinction between malignant mesothelioma and pulmonary adenocarcinoma: A critical evaluation of new antibodies. *J Clin Pathol* 55:662–668.
28. Graves EE, Culver JP, Ripoll J, Weissleder R, Ntziachristos V (2004) Singular-value analysis and optimization of experimental parameters in fluorescence molecular tomography. *J Opt Soc Am A Opt Image Sci Vis* 21:231–241.
29. Ntziachristos V, Yodh AG, Schnall M, Chance B (2000) Concurrent MRI and diffuse optical tomography of breast after indocyanine green enhancement. *Proc Natl Acad Sci USA* 97:2767–2772.